

Rapid Detection of Strong Correlation with Machine Learning for Transition-Metal Complex High-Throughput Screening

Fang Liu, Chenru Duan, and Heather J. Kulik*



Cite This: *J. Phys. Chem. Lett.* 2020, 11, 8067–8076



Read Online

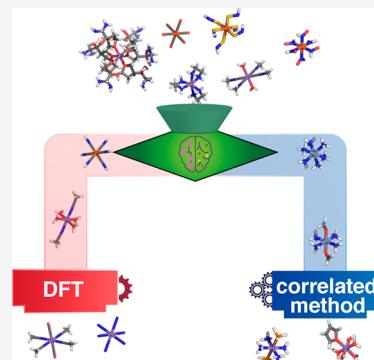
ACCESS |

Metrics & More

Article Recommendations

SI Supporting Information

ABSTRACT: Despite its widespread use in chemical discovery, approximate density functional theory (DFT) is poorly suited to many targets, such as those containing open-shell, 3d transition metals that can be expected to have strong multireference (MR) character. For discovery workflows to be predictive, we need automated, low-cost methods that can distinguish the regions of chemical space where DFT should be applied from those where it should not. We curate more than 4800 open-shell transition-metal complexes up to hundreds of atoms in size from prior high-throughput DFT studies and evaluate affordable, finite-temperature DFT fractional occupation number (FON)-based MR diagnostics. We show that intuitive measures of strong correlation (i.e., the HOMO–LUMO gap) are not predictive of MR character as judged by FON-based diagnostics. Analysis of independently trained machine learning (ML) models to predict HOMO–LUMO gaps and FON-based diagnostics reveals differences in the metal and ligand sensitivity of the two quantities. We use our trained ML models to rapidly evaluate MR character over a space of ~187000 theoretical complexes, identifying large-scale trends in spin-state-dependent MR character and finding small HOMO–LUMO gap complexes while ensuring low MR character.



High-throughput computational screening is essential in the discovery of new molecules^{1–5} and materials.^{6–9} For these efforts, density functional theory (DFT) with approximate exchange-correlation functionals is nearly exclusively employed to ensure the low computational cost and ease of automation needed for the study of thousands of molecules with tens to hundreds of atoms. Open-shell transition-metal complexes that are useful catalysts^{4,10–16} and functional materials^{17–21} exemplify both the promise and outstanding challenges for computational screening. The properties of these molecules can be tuned by variation of ligand chemistry, which in turn influences the relative stability of spin and oxidation states,^{5,22} highlighting the opportunities for large-scale screening in their design.^{5,23,24}

In small-scale studies, careful benchmarking of the computational method is possible,^{25–28} including the detection of strong correlation that motivates the use of multireference (MR) electronic structure techniques.^{29–31} However, high-scaling methods have been limited in large-scale screening contexts to small organic molecules.^{32,33} The development of machine learning (ML) property prediction models^{23,34–38} and interatomic potentials^{39–43} compounds the challenges associated with screening, both by motivating the generation of large data sets and by magnifying the impact of electronic structure biases when they are learned by an ML model.

First-row open-shell transition-metal complexes with nearly degenerate 3d orbitals can be expected to exhibit strong correlation.^{25–27,44,45} Here, approximate DFT will fail,^{46–49} and the accurate treatment of dynamic and static correlation in

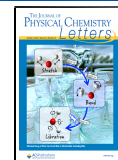
larger transition-metal complexes remains an active area of research.^{29–31} For small, well-studied molecules (e.g., the chromium dimer^{50–53}), the effects of strong correlation are understood, but target complexes in chemical discovery lack literature precedent for guiding expectations of MR character. To advance large-scale screening in these spaces, it is necessary to develop tools for detecting strong correlation that can be integrated into existing DFT workflows at no greater complexity or computational cost.

While numerous MR diagnostics have been developed,^{54–65} we focus on diagnostics^{63–65} based on fractional occupation numbers (FONs) that can be obtained from computationally affordable finite-temperature DFT⁶⁶ (FT-DFT). Because electron correlation can be attributed alternately to both dynamical and nondynamical (i.e., MR) contributions,^{67–69} Matito and co-workers^{63,64} have derived expressions for dynamical, I_D , and nondynamical, I_{ND} , quantities. The I_D is computed from the occupation, n , of orbital i with spin σ as^{63,64}:

Received: July 25, 2020

Accepted: August 31, 2020

Published: August 31, 2020



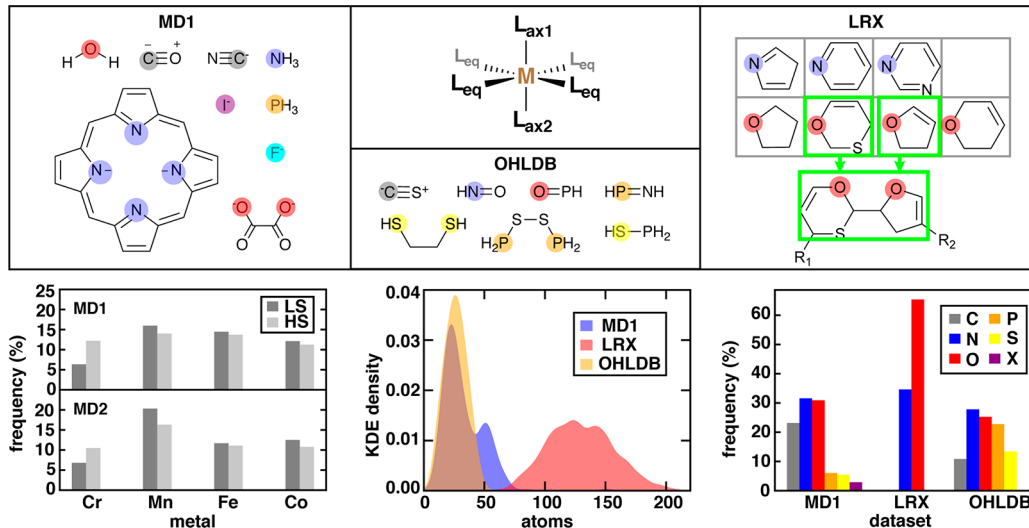


Figure 1. Properties of the octahedral complexes in the data sets studied in this work (MD1, LRX, OHLDB, and MD2, which is the union of the other data sets). The top panels show a schematic of a transition-metal complex illustrating possible unique (one equatorial, L_{eq} , and up to two axial, L_{ax1} and L_{ax2}) and representative ligands. Ligand atoms that coordinate the metal are shaded with circles colored by element: O in red, N in blue, P in orange, S in yellow, C in gray, F in cyan, and I in purple. Bar graph of the metal identity and spin state (HS, dark gray; LS, light gray) of MD1 and MD2 (bottom left). Kernel density estimation (KDE) of the distribution of the size of complexes in MD1, LRX, and OHLDB (bottom center). Clustered bar graph for the connecting atom identity (X indicates any halide) in MD1, LRX, and OHLDB (bottom right).

$$I_D = \frac{1}{4} \sum_{\sigma,i} [n_i^\sigma (1 - n_i^\sigma)]^{1/2} - \frac{1}{2} \sum_{\sigma,i} n_i^\sigma (1 - n_i^\sigma) \quad (1)$$

The nondynamical^{63,64} I_{ND} is:

$$I_{ND} = \frac{1}{2} \sum_{\sigma,i} n_i^\sigma (1 - n_i^\sigma) \quad (2)$$

where larger I_{ND} values can be used as an indicator of MR character.^{33,63,64,70} The ratio, r_{ND} , of the I_{ND} to the total correlation (i.e., $I_D + I_{ND}$) has been proposed by Martin and co-workers⁶⁷ as a size-intensive variant of the MR diagnostics developed by Matito and co-workers:^{63,64}

$$r_{ND} = \frac{I_{ND}}{I_D + I_{ND}} \quad (3)$$

where larger values of r_{ND} have been shown to be³³ indicative of strong MR character.

Grimme and co-workers have developed the closely related fractional occupation density (FOD),⁶⁵ which can be integrated over all space to yield N_{FOD} , a size-extensive FON-based diagnostic for quantifying nondynamical correlation. We focus on the size-intensive r_{ND} , and we demonstrate our approach is general to both size-extensive, FON-based diagnostics (i.e., I_{ND} and N_{FOD}) and approximately size-intensive quantities that we obtain by normalizing with the number of valence electrons, n_{ve} (i.e., I_{ND}/n_{ve} and N_{FOD}/n_{ve}). We have previously shown³³ I_{ND} , r_{ND} , and N_{FOD} to yield comparable predictions of relative MR character (for I_{ND} vs N_{FOD} , Pearson's $r = 0.99$, and for I_{ND} vs r_{ND} , Pearson's $r = 0.91$) that were reasonable predictors of MR effects (i.e., the degree of recovery of the correlation energy from truncations of coupled cluster theory). In the work presented here, our goal is to assess MR character across transition-metal complexes widely varying in size, which motivates the use of the DFT-cost, approximately size-intensive r_{ND} diagnostic.

While FON-based diagnostics have demonstrated promise^{65,70} for the quantitative prediction of MR character in

studies of small sets of transition-metal complexes, they have yet to be incorporated in large-scale, high-throughput screening. We thus first curated a diverse set of 4865 mononuclear octahedral transition-metal complexes from six prior studies^{71–76} and assessed their MR character with FON-based diagnostics. We accelerated the calculation of FON-based diagnostics by leveraging the existing converged geometries and wave functions from fixed-occupation DFT for the FT-DFT⁶⁶ calculations (see Computational Details). All complexes contain a midrow transition metal in one of two oxidation states [i.e., M(II)/M(III), where M = Cr, Mn, Fe, or Co] in its high-spin (HS) or low-spin (LS) state (see Computational Details). Over all sets considered, the metals and spin states are evenly distributed, with only somewhat fewer Cr complexes (Figure 1).

A 2305-complex subset (MD1) from four of the studies^{71–74} consists of small to midsized complexes constructed from common ligands originally to study their spin^{71,72,74} or redox⁷³ properties (Figure 1 and Table S1). The MD1 complexes are around 50 atoms in size and primarily contain first-row (i.e., C, N, or O) coordinating atoms (Figure 1 and Table S1). The larger 4865-complex MD2 data set consists of all complexes in MD1 along with (i) complexes of heuristically enumerated ligands (OHLDB⁷⁶) and (ii) large bidentate redox (LRX⁷⁵) complexes (Figure 1 and Tables S1 and S2). The OHLDB complexes are smaller (~25 atoms) and have more diverse coordinating atoms and bonding than those in MD1, whereas the LRX complexes are much larger (i.e., ≤ 200 atoms) but have fewer coordinating atom types and more uniform bonding (Figure 1 and Table S1). The diversity of size and bonding in MD2 means that we are less likely to have information from prior experiment or computation in comparison to the more common complexes in MD1.

Over the MD1 data set, the r_{ND} values span a large range (0.10–0.66), suggesting a significant variation in the extent of strong correlation, although all complexes are derived from common ligands (Figure 2). The MD2 data set has a comparable r_{ND} range, despite its greater diversity in both

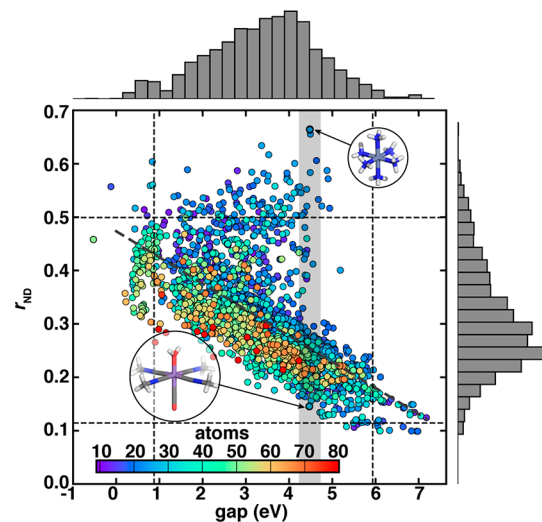


Figure 2. Scatter plot of the two-dimensional distribution of the HOMO–LUMO gap and r_{ND} values for MD1 complexes. The symbols are colored by the number of atoms in the complex, as indicated in the inset color bar. One-dimensional histograms are aligned with the respective axes. Vertical and horizontal dashed lines indicate two standard deviations around the mean. The correlation between r_{ND} and gap is indicated with a gray dashed line ($R^2 = 0.413$). A gray shaded region (HOMO–LUMO gap = 4.48 ± 0.25 eV) is shown with the complexes with the highest [$\text{LS Cr}^{\text{II}}(\text{NH}_3)_6$] and lowest [$\text{HS Mn}^{\text{II}}(\text{misc})_4(\text{H}_2\text{O})(\text{CO})$] r_{ND} values outlined and shown with inset structures.

ligand chemistry and complex size (Figure S1). The size-extensive diagnostics (i.e., I_{ND} and N_{FOD}) differ significantly between MD1 and MD2, but the comparable behavior of r_{ND} as well as n_{ve} -normalized quantities (i.e., $I_{\text{ND}}/n_{\text{ve}}$ and $N_{\text{FOD}}/n_{\text{ve}}$) supports our focus on a size-intensive diagnostic (Figures S2–S5).

One might expect it to be straightforward to predict MR character from fixed-occupation DFT calculations, e.g., by the size of the gap between the highest occupied and lowest unoccupied molecular orbitals (HOMO–LUMO gap). The HOMO–LUMO gaps span a wide range (0–7 eV) over the MD1 set, but they only weakly correlate ($R^2 = 0.41$) with the r_{ND} diagnostic (Figure 2). Still, the relationship follows expectations, with the smallest HOMO–LUMO gap complexes having more MR character (i.e., higher r_{ND}) than the complexes with the largest HOMO–LUMO gaps. Nevertheless, this relationship worsens over the diverse MD2 set ($R^2 = 0.17$), despite HOMO–LUMO gap and r_{ND} ranges comparable to those of MD1 (Figure S1). We might expect this to be due to the greater size dependence of the HOMO–LUMO gap than r_{ND} , but correlations for both sets are still weak ($R^2 < 0.6$) with size-extensive (i.e., I_{ND} and N_{FOD}) MR diagnostics (Figure 2 and Figures S2, S4, and S6 and Table S3). The relative HOMO–LUMO gap [i.e., $(H - L)/(H + L)$, where H and L are the HOMO and LUMO eigenvalues] has been suggested⁷⁷ as a good proxy for “type B” static correlation (e.g., in Be-like ions), but the correlation between relative gap and MR diagnostics is also poor (Figures S7–S11). Indeed, for near-degenerate orbitals in open-shell transition-metal complexes, we should expect the MR character and thus FON-based MR diagnostics such as r_{ND} to have significant contributions from the valence states in a manner that may

not be readily captured by considering only the HOMO and LUMO.

A closely related question is whether the FON-based MR diagnostics such as r_{ND} are suitable for predicting MR effects. While recent work has supported their reasonable performance in transition-metal chemistry,⁷⁰ we recently showed³³ that MR effects in small organic molecules, as judged through the degree of recovery of the correlation energy, were most faithfully predicted by wave function-theory (WFT)-based MR diagnostics (e.g., from CASSCF). For the thousands of transition-metal complexes with roughly 25–200 atoms in this work that mimic real-world lead compounds in chemical discovery, full evaluation of WFT-based diagnostics is not tractable. Still, we evaluated both WFT-based diagnostics and the recovery of the correlation energy over representative, small transition-metal complexes with low, intermediate, or high r_{ND} values (Tables S4 and S5). Over this representative set, we observe that a low or high r_{ND} value correctly classifies the complexes as relatively low or high MR character, respectively (Tables S4 and S5).

Thus, given the weak relationship between the HOMO–LUMO gap and MR character, we investigated what gives rise to low or high MR character in MD1 for small (i.e., 0.88 ± 0.25 eV) and large (i.e., 4.48 ± 0.25 eV) gap values. Many of the 276 large gap complexes have expectedly low r_{ND} values, including a HS $\text{Mn}^{\text{II}}(\text{misc})_4(\text{H}_2\text{O})(\text{CO})$ with an r_{ND} value (0.13) in the bottom 2% for MD1 (Figure 2). Conversely, LS $\text{Cr}^{\text{II}}(\text{NH}_3)_6$ has the highest r_{ND} (0.66) in all of MD1, despite its large HOMO–LUMO gap, suggesting that LS Cr complexes might have especially high MR character (Figure 2). For the 66 small HOMO–LUMO gap MD1 complexes, expectedly high r_{ND} values are observed [i.e., for LS $\text{Mn}^{\text{III}}(\text{H}_2\text{O})_5(\text{furan})$, $r_{\text{ND}} = 0.60$] but unexpectedly low MR character is, as well (i.e., for LS $\text{Mn}^{\text{III}}(\text{pisc})_6$, $r_{\text{ND}} = 0.27$) as well as (Figure 2). Given the higher diversity of MD2, distinct deviations are observed, including low r_{ND} and gaps (e.g., in an LRX O-coordinating bidentate homoleptic HS Mn^{III} complex, $r_{\text{ND}} = 0.22$ and gap = 0.3 eV) even for complexes with similar metal and coordinating atoms to much higher r_{ND} MD1 points (Figure S1). Despite the intuitive link between MR character 206 and HOMO–LUMO gap, metal identity (e.g., Cr) and spin 207 state (e.g., LS) exceptions are apparent, motivating the development of ML models capable of encoding these complex relationships.

We trained ML (i.e., artificial neural network, ANN, and kernel ridge regression, KRR) models to independently predict FON-based diagnostics (e.g., r_{ND}) and frontier orbital energetics, i.e., the HOMO level and HOMO–LUMO gap (see Computational Details and Text S1). We used revised autocorrelation (RAC)^{78,79} functions as input features, which have previously been demonstrated for predictive, geometry-free estimation of frontier orbital energies to good (~ 0.1 –0.2 eV) accuracy (Text S2).^{73,78} A geometry-free representation is preferred for transition-metal chemistry because it requires no prior precise geometric information for making the prediction, reducing the size of the training data set required and the cost of feature generation, yet can still be used to predict properties dependent on geometric changes (e.g., catalyst reaction energetics⁸⁰). RACs are products and differences on the molecular graph of heuristic properties (i.e., topology, identity, nuclear charge, covalent radius, or electronegativity) of pairs of atoms a fixed number, d , bonds apart (see Computational Details and Text S2). For the ML models trained on the MD2

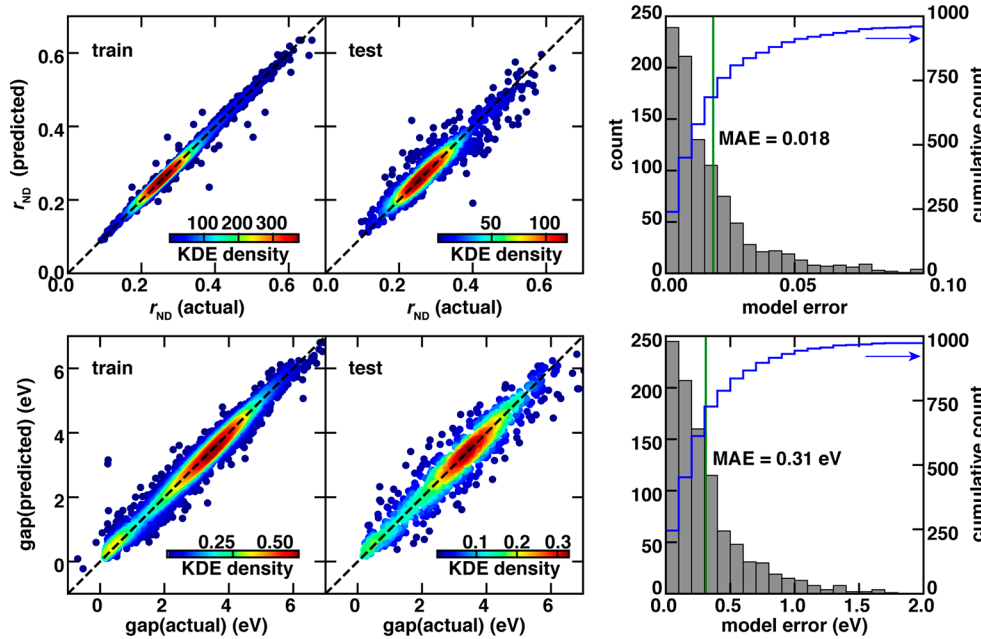


Figure 3. ANN model performance for predicting r_{ND} (top) and HOMO–LUMO gap (bottom) for the MD2 data set. Parity plots (left) of actual vs predicted values for train and test data points colored by kernel density estimation (KDE) density values, as indicated by inset color bars. In all cases, a black dashed parity line is also shown. Distributions (right) of absolute test set model errors for r_{ND} (unitless, bins of 0.005) and HOMO–LUMO gap (in eV, bins of 0.1 eV) with the MAE annotated as green vertical bars and the cumulative count shown in blue according to the axis on the right.

data set with RAC features, ANN model test mean absolute errors (MAEs, 0.26 eV for HOMO and 0.31 eV for the HOMO–LUMO gap) are similar to those for MD1 or prior work^{10,14} on MD1 subsets, increasing only slightly despite being obtained on a much more diverse data set (Figure 3 and Table S6 and Figures S12 and S13). As shown in prior work,^{75,81} the greater diversity in size and ligand chemistry of MD2 complexes means a model trained on only MD1 would not be expected to be predictive on MD2.

It is not evident *a priori* if FON-based diagnostics that are derived from temperature-dependent properties obtained with FT-DFT are as easily learned quantities as the fixed-occupation DFT frontier orbital energies. The ML model trained on MD2 to predict r_{ND} does exhibit performance that is as good as that for the HOMO–LUMO gap, with the ANN test MAE for r_{ND} (0.018) corresponding to a smaller mean absolute percent error (3%) over the r_{ND} range than that (4%) for the HOMO–LUMO gap (Figure 3). The r_{ND} MAE represents a modest error in comparison to the variation between diagnostic values associated with low (e.g., $r_{\text{ND}} < 0.3$) or high (e.g., $r_{\text{ND}} > 0.5$) MR character (Figure 3 and Table S6 and Figure S12). In comparison to predicting r_{ND} with a linear mapping from the HOMO–LUMO gap, the ANN performance is vastly superior ($R^2 = 0.456$ for linear vs $R^2 = 0.942$ for ANN) and test MAEs are significantly lower (Figures S14 and S15 and Table S7).

Interpretation of the character of informative RACs provides insight^{78,82} into why MR character (i.e., r_{ND}) and HOMO–LUMO gap differ among these transition-metal complexes. To identify the most informative features,^{78,82} we pair feature selection with the training of KRR models,^{73,78} which achieves similar performance to that obtained with ANNs (Tables S6 and S8–S14 and Figures S16 and S17). Analysis of feature sets selected by training on MD1 confirms that distinct properties are important for predicting r_{ND} (i.e., $r_{\text{ND}-28}$) versus predicting

the HOMO–LUMO gap (gap-28) or HOMO level (Figure 4 and Figure S18 and Tables S9, S10, and S15–S17). Although the $r_{\text{ND}-28}$ and gap-28 feature sets are the same size, the gap subset contains a larger portion of global features (43% vs 32%) than the r_{ND} subset (Figure 4 and Tables S16 and S17). Electronegativity-based RACs are more crucial for predicting MR character (25% of $r_{\text{ND}-28}$ vs 11% of gap-28) as is the metal nuclear charge, whereas global, covalent radius-based features present only in gap-28 highlight the greater size dependence of the HOMO–LUMO gap (Figure 4 and Tables S16 and S17). Qualitatively similar trends are observed for models trained on MD2, although the size of the gap-selected feature set grows significantly due to the greater diversity of ligand chemistry in the set (Tables S12 and S13).

Although over our data sets we had observed a weak correlation between the gap and MR character, these feature-selected subsets provide explicit design principles over MD1, i.e., to separately tailor the gap and MR character by focusing on ligand size-based versus metal-based properties. For example, the LS $\text{Fe}^{\text{III}}(\text{CO})_4(\text{H}_2\text{O})(\text{misc})$ and $\text{Cr}^{\text{II}}(\text{CO})_4(\text{H}_2\text{O})(\text{misc})$ complexes differ only in their metal center and have comparable (Fe^{III} : 2.73 eV; Cr^{II} : 2.87 eV) HOMO–LUMO gaps (Figure 4). This difference instead has a profound effect on MR character, with the Cr^{II} complex having a high r_{ND} (0.55), whereas the Fe^{III} complex r_{ND} (0.33) is lower (Figure 4). Conversely, replacing water ligands with larger furan ligands in HS homoleptic Fe^{III} or Mn^{III} complexes has a modest effect on MR character (r_{ND} from 0.34 to 0.40 in Fe^{III}) because the immediate coordinating environment is unchanged, whereas the increased ligand size reduces the gap substantially, in Fe^{III} by 3.44 eV (Figure 4).

To demonstrate the value of our approach in a context representative of chemical discovery efforts, we applied the gap and r_{ND} ANN models trained on MD2 to a space of 187200 transition-metal complexes. This space of theoretical com-

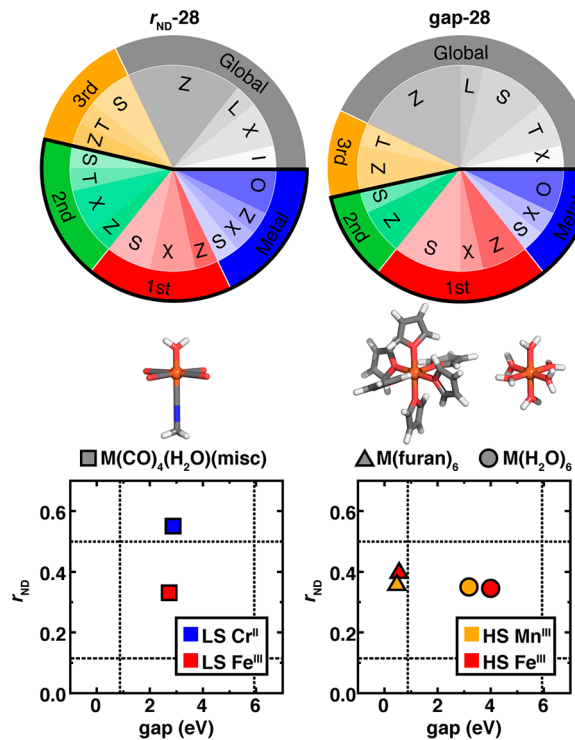


Figure 4. Pie charts of the features selected by random forest-ranked recursive feature addition (RF-RFA) on the MD1 data set for HOMO–LUMO gap (gap-28, left) and the r_{ND} diagnostic ($r_{\text{ND}}\text{-28}$, right). Features are grouped by the most metal-distant atoms: metal in blue, first coordination sphere in red, second coordination sphere in green, third coordination sphere in orange, and more distant, global features in gray (a black outline is used to group the first three categories). Within each distance category, the property (i.e., χ , S, T, Z, or I) is also indicated, with the oxidation/spin state (O) assigned as metal-local and the ligand charge (L) assigned as global. HOMO–LUMO gap (eV) and r_{ND} values (unitless) (bottom panels) illustrating the stronger effect of metal identity on r_{ND} (left) and of nonlocal features on gap (right). Vertical and horizontal dashed lines indicate two standard deviations around the mean gap or r_{ND} for MD1. The representative complex structures are shown along with their symbol legends above the plots.

plexes contains HS and LS M(II/III) ($M = \text{Cr}, \text{Mn}, \text{Fe}, \text{or Co}$) centers in complex with 36 unique ligands derived from the original MD1 data set. Although all ligand identities were in the ANN training data, only 1% (1836) of the complexes were, and thus the theoretical complexes have properties (e.g., size and charge) distinct from those of the original data set (Tables S18–S20 and Figures S19 and S20).

Over this large theoretical complex space, we investigate what the ML model has learned about how MR character is influenced by transition-metal complex chemistry (i.e., spin state, metal, and ligand). Spin-state ordering calculations in particular are known to be sensitive to method choice,^{82–88} especially due to the lack of error cancellation when the degree of correlation recovery differs between spin states.^{30,88–91} It has been observed, for example, in small-scale studies of organic molecules^{68,92} and some first-row transition-metal complexes⁸⁸ that LS states are more degenerate and thus have higher MR character than HS states.

Although some metal centers in our large-scale set follow this trend, others do not. The Cr and Mn complexes exhibit an increase in MR character from HS to LS for both r_{ND} and other FON-based diagnostics, whereas Fe and Co complexes have

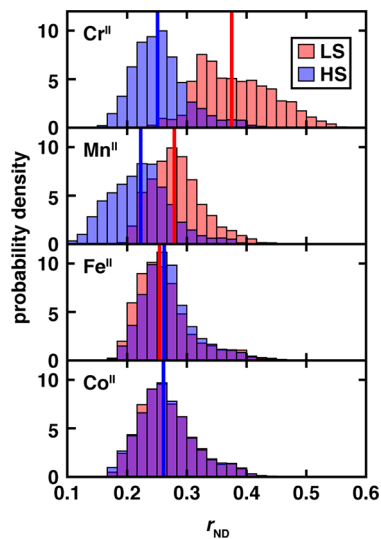


Figure 5. Normalized probability density distribution of r_{ND} (unitless, bin size of 0.0167) as predicted by the ANN for the 93600 M(II) complexes ($M = \text{Cr}, \text{Mn}, \text{Fe}, \text{or Co}$) in the full compound space. There are 11700 complexes for each M(II) spin state. The histograms are colored by spin (red for low spin, LS, and blue for high spin, HS). The median of each distribution is indicated by a vertical line with the same corresponding color.

limited spin-state dependence (Figure 5 and Figures S21–S26). For the HS complexes in either oxidation state, all metals have comparable diagnostic (e.g., r_{ND}) distributions, suggesting the HS–LS MR character difference for Cr/Mn arises primarily from increased LS MR character (Figure 5 and Figures S22–S26). Indeed, for the Cr/Mn complexes with the greatest HS–LS MR character difference, the LS r_{ND} is very high while the HS r_{ND} is somewhat lower than the overall average (Figure S27). The ligands that most frequently appear in these complexes are small, sometimes charged species (e.g., NH₃, OH[−], S^{2−}, and CN[−]) with intermediate field strengths (Figure S22). Although MR character is strongly dependent on the spin state and metal, subtle differences in chemistry are apparent between ligands that frequently occur in low-MR character complexes (e.g., NH₂CH₃) and those (e.g., NCO[−]) in complexes with high MR character (Figures S28 and S29).

Within the space of theoretical complexes, independent ML models also make it possible to target optimal DFT properties (e.g., for the HOMO–LUMO gap) while identifying DFT-safe portions of chemical space by avoiding complexes with high MR character. The ML model-predicted MR character and HOMO–LUMO gap vary widely but are, as in the training data, weakly correlated (Figures S30–S34). These trends are expected to be robust because ANN model test errors are modest, but we focus our analysis on low uncertainty points in the theoretical space as quantified by those with the smallest distances in ANN model latent space⁸¹ (Text S3 and Figures S35 and S36).

Given the expectation^{68,93} that small HOMO–LUMO gap complexes will have strong MR character, we sought to identify chemical motifs that break this relationship (Figure 6). For the complexes with confidently assigned small HOMO–LUMO gaps (<1 eV) and below-average MR character ($r_{\text{ND}} < 0.3$), clear patterns emerge (Figure 6). One in three (134 of 403) of these target complexes is from the same family of HS Co^{III} or Mn^{III} complexes with equatorial substituted-pyridine ligands and axial weak-field ligands that thus reside in a narrow region

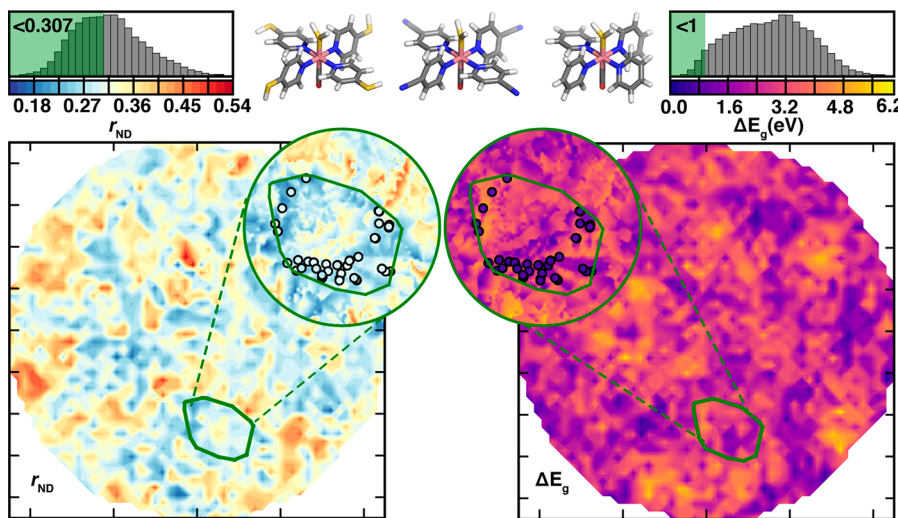


Figure 6. Properties of the theoretical complex space colored by ANN-predicted r_{ND} (left, unitless) and HOMO–LUMO gap (right, ΔE_g in eV). One-dimensional histograms (top) of r_{ND} and HOMO–LUMO gap are aligned with their respective color bars and target zones ($r_{ND} < 0.307$, and HOMO–LUMO gap < 1 eV) shaded in green. t-Distributed stochastic neighbor embedding plots (bottom) are shown and colored as indicated in the top inset color bar. The convex hull of a family of 3744 octahedral complexes with functionalized pyridinyl ligands is indicated by a green outline. Inset circles show a close-up of this convex hull with discrete complexes in circles (representative complexes shown in the top middle of the plot): the 134 complexes within target ranges of r_{ND} and HOMO–LUMO gap and low (bottom 10%) distance in latent space to training data.

of the complex space (Figure 6 and Tables S21 and S22 and Figures S37 and S38). Conversely, nearby complexes (e.g., with strong-field equatorial carbonyl ligands) also have small gaps but instead have relatively high MR character (Figure 6 and Figure S39 and Table S23). In the future, these ANN models could be paired with optimization strategies^{72,75,94,95} for the continued discovery of DFT-safe islands of complexes with optimal properties along with low MR character and high ML model confidence from even larger spaces of theoretical transition-metal complexes.

In summary, we have demonstrated a low-cost approach that can be integrated into current DFT high-throughput screening workflows for open-shell transition-metal complexes and materials. Over a curated set of nearly 5000 open-shell transition-metal complexes from prior high-throughput DFT studies, we evaluated MR character from FON-based diagnostics. Because intuitive measures of strong correlation (i.e., the HOMO–LUMO gap) were not predictive of these FON-based diagnostics, we trained ML models to separately predict frontier orbital energies (i.e., the HOMO–LUMO gap) and FON-based diagnostics. Models trained to predict FON-based diagnostics were as predictive as models trained to predict fixed-occupation DFT properties. Analysis of the important features for model prediction revealed that MR character is more metal-sensitive, whereas the HOMO–LUMO gap is more ligand-sensitive. We used these principles to identify opportunities for tailoring the two quantities independently. We demonstrated the promise of our ANN models for chemical discovery efforts by evaluating MR character over a space of more than 187000 theoretical complexes, identifying large-scale trends in spin-state-dependent MR character, and discovering small HOMO–LUMO gap complexes with low MR character. Natural next steps in this work will be to apply recently developed⁹⁶ geometry-dependent adaptations of RACs to build models that also can predict the dependence of MR character upon distortion of chemical bonds in transition-metal complexes. While the current work has been demonstrated on affordable DFT-based

diagnostics, we expect the approach of accelerating discovery of new materials with low MR character to be equally applicable in cases in which typically more accurate WFT-based MR diagnostics can be generated or predicted^{33,96} on these relatively large transition-metal complexes. We expect this approach to be valuable both for the practical goal of identifying where DFT level workflows are sufficiently robust and for discovering strongly correlated molecules as test cases for more advanced electronic structure methods.

COMPUTATIONAL DETAILS

Data Sets and Calculations. We curated a data set of 4865 mononuclear octahedral transition-metal complexes generated in six prior studies^{71–76} using fixed-occupation DFT geometry optimizations in TeraChem^{97,98} automated with molSimplify.^{99,100} All sets used the same HS and LS multiplicity definitions in midrow M(III)/M(II) complexes as follows: quintet-singlet for both d⁴ Mn(III)/Cr(II) and d⁶ Co(III)/Fe(II), sextet-doublet for d⁵ Fe(III)/Mn(II), and quartet-doublet for both d³ Cr(III) and d⁷ Co(II).

We automated the calculation of FT-DFT⁶⁶ MR diagnostics^{63–65} (e.g., r_{ND} and N_{FOD}) with MultirefPredict¹⁰¹ and the QCEngine¹⁰² interface to TeraChem^{97,98} on the curated structures from prior work. For the sake of consistency, all DFT calculations employed the B3LYP^{103–105} hybrid functional with LANL2DZ¹⁰⁶ effective core potentials for the transition metals, I, or Br and the 6-31G* basis for the remaining atoms. Level shifting¹⁰⁷ was used in unrestricted (i.e., nonsinglet) calculations with a uniform 0.25 au value for FT-DFT and most prior fixed-occupation DFT calculations (Table S24). The FT-DFT calculations employed the recommended⁶⁵ temperature for B3LYP (9000 K) with Fermi–Dirac smearing and were initiated from fixed-occupation DFT wave functions^{71–76} when available (Text S4 and Tables S24 and S25).

All complexes were filtered prior to analysis and ML model training in a four-step process. Complexes for which FT-DFT calculations did not converge were first eliminated followed by

those with positive (i.e., unbound) or unreported majority-spin HOMO levels from fixed-occupation DFT (Text S4 and Table S26). Geometries were next checked⁷³ for preserved connectivity and quality, and finally, highly symmetry-broken fixed-occupation DFT (i.e., with $\langle S^2 \rangle$ deviations from $S(S + 1) > 1$) results were excluded (Tables S26 and S27).

ML Models. KRR and ANN models were trained on all 151 RACs (i.e., $42d + 30$ with a cutoff of $d = 3$ after elimination of invariant RACs) along with three overall (i.e., oxidation state, denticity, and total charge)⁷⁸ complex features as well as feature-selected subsets (Text S2). Hyperparameter optimization for all models was carried out with Hyperopt¹⁰⁸ using a random 80% train/20% test split, with 20% of the training set (16% overall) set aside as the validation subset for hyperparameter selection. Input features and outputs were normalized over the training set to have zero mean and unit variance. As in prior work,⁷³ KRR model feature selection was carried out with random forest¹⁰⁹-ranked recursive feature addition (RF-RFA).¹¹⁰ With each feature addition, the KRR model was trained (i.e., to select regularization strength and kernel width) and judged on the KRR model R^2 for the validation set. RF-RFA was stopped when no improvement in R^2 was observed. Final KRR models were implemented in scikit-learn,¹¹¹ trained on the full (80% overall) training set, and tested on the 20% test set (Table S28).

Fully connected ANN models were trained using Keras¹¹² with TensorFlow¹¹³ as the backend and Hyperopt¹⁰⁸ for hyperparameter selection (Table S29). Each ANN model was trained with batch optimization for 1000 epochs with early stopping when no more performance improvement was observed, and we included dropout regularization^{114,115} to avoid overfitting (Table S30). The optimal ANN topology for all models consisted of 512 nodes per layer with either two (e.g., for the HOMO level) or three (e.g., for HOMO–LUMO gap and r_{ND}) hidden layers (Table S30).

ASSOCIATED CONTENT

Supporting Information

The Supporting Information is available free of charge at <https://pubs.acs.org/doi/10.1021/acs.jpcllett.0c02288>.

Statistics of denticity, size, and net charge of complexes in data sets; correlation between gap and r_{ND} for MD2; correlation between gap and MR diagnostics (r_{ND} , I_{ND} , I_{ND}/n_{ve} , N_{FOD} , and N_{FOD}/n_{ve}) for MD1 and MD2; KDE of r_{ND} and gap for molecules of different sizes; regression parameters for molecules of different sizes; definition of HOMO and LUMO; extended description of RAC featurization; performance of ML models for HOMO–LUMO gap and r_{ND} ; train and test set performance of KRR and ANN models trained on MD1 and MD2; MD1; linear model for predicting r_{ND} from DFT- or ANN-predicted gap; additional linear, KRR, and ANN model performance statistics; performance of ML models for HOMO level, I_{ND} , and N_{FOD} ; optimal KRR features for HOMO prediction and gap prediction of MD1 and MD2; pie chart of the optimal features for HOMO level prediction of MD1; statistics on HOMO-S2, gap-28, and r_{ND} -28 feature sets; ligands used for building the theoretical complex space; allowed ligand combinations and spin/oxidation combinations in the theoretical complex space; distribution of sizes in the theoretical complex space; distribution of theoretical

space M(III) r_{ND} values; difference of theoretical space HS and LS r_{ND} values; distribution of theoretical space M(II)/M(III) I_{ND} , I_{ND}/n_{ve} , N_{FOD} , and N_{FOD}/n_{ve} values; contributions to high HS–LS r_{ND} difference complexes; ligand types in the top 5% and bottom 5% of r_{ND} in the theoretical complex space; correlation between gap or relative gap and MR diagnostics (r_{ND} , I_{ND} , N_{FOD} , I_{ND}/n_{ve} , and N_{FOD}/n_{ve}) for 187000 theoretical complexes; representative transition-metal complexes for which $\%E_{corr}[(T)]$ and WFT-based MR diagnostics were obtained; details of latent space distance evaluation; distribution of gap latent space distances and r_{ND} latent space distances over theoretical space; ligands in the target leads inside the convex hull of theoretical space; metals in the target leads inside the convex hull of theoretical space; r_{ND} distribution and HOMO–LUMO distribution of target leads inside the convex hull; convex hull compounds with large r_{ND} values; attributes of ligands in convex hull compounds with large r_{ND} values; summary of the size of data sets after each stage of refinement; additional details about finite-temperature calculations; number of core orbitals for different elements; summary of wave function-related information for each data set; geometry check cutoffs for data refinement; optimal hyperparameters for KRR models in this work; hyperspace for ANN hyperparameter optimization; and optimal hyperparameters for ANN models in this work (PDF)

Total energies in fixed-occupation and finite-temperature DFT, MR diagnostics, and orbital energies in fixed-occupation DFT of all molecules in the six raw data sets and the refined data sets MD1 and MD2; list of molecules eliminated during MD2 set curation; list of molecules in MD2 lacking fixed-occupation DFT wave function information from previous studies; ANN-predicted MR diagnostics and orbital energies for the design space; list of unique ligands in MD1 and MD2; ANN and KRR models trained on the MD1 and MD2 training set; and geometries of all molecules in MD2 (ZIP)

AUTHOR INFORMATION

Corresponding Author

Heather J. Kulik – Department of Chemical Engineering, Massachusetts Institute of Technology, Cambridge, Massachusetts 02139, United States;  orcid.org/0000-0001-9342-0191; Phone: 617-253-4584; Email: hjkulik@mit.edu

Authors

Fang Liu – Department of Chemical Engineering, Massachusetts Institute of Technology, Cambridge, Massachusetts 02139, United States;  orcid.org/0000-0003-1322-4997

Chenru Duan – Department of Chemical Engineering and Department of Chemistry, Massachusetts Institute of Technology, Cambridge, Massachusetts 02139, United States;  orcid.org/0000-0003-2592-4237

Complete contact information is available at:

<https://pubs.acs.org/doi/10.1021/acs.jpcllett.0c02288>

Notes

The authors declare no competing financial interest.

ACKNOWLEDGMENTS

The authors acknowledge primary support (for F.L. and H.J.K.) by the U.S. Department of Energy under Grant DE-SC0018096 as well as a MolSSI fellowship (Grant ACI-1547580) to F.L. Additional support for data set generation was provided by the Office of Naval Research under Grants N00014-18-1-2434 and N00014-20-1-2150 (to C.D. and H.J.K.) and DARPA under Grant D18AP00039 (to C.D. and H.J.K.). This work made use of Department of Defense HPCMP computing resources. This work was also carried out in part using computational resources from the Extreme Science and Engineering Discovery Environment (XSEDE), which is supported by National Science Foundation Grant ACI-1548562. H.J.K. holds a Career Award at the Scientific Interface from the Burroughs Wellcome Fund and an AAAS Marion Milligan Mason Award, which supported this work. The authors thank Adam H. Steeves for providing a critical reading of the manuscript. The authors would also like to thank Aditya Nandy for providing helpful discussions and scripts.

REFERENCES

- (1) Shu, Y.; Levine, B. G. Simulated Evolution of Fluorophores for Light Emitting Diodes. *J. Chem. Phys.* **2015**, *142*, 104104.
- (2) Gomez-Bombarelli, R.; Aguilera-Iparraguirre, J.; Hirzel, T. D.; Duvenaud, D.; Maclaurin, D.; Blood-Forsythe, M. A.; Chae, H. S.; Einzinger, M.; Ha, D. G.; Wu, T.; et al. Design of Efficient Molecular Organic Light-Emitting Diodes by a High-Throughput Virtual Screening and Experimental Approach. *Nat. Mater.* **2016**, *15*, 1120–1127.
- (3) Kanal, I. Y.; Owens, S. G.; Bechtel, J. S.; Hutchison, G. R. Efficient Computational Screening of Organic Polymer Photovoltaics. *J. Phys. Chem. Lett.* **2013**, *4*, 1613–1623.
- (4) Vogiatzis, K. D.; Polynski, M. V.; Kirkland, J. K.; Townsend, J.; Hashemi, A.; Liu, C.; Pidko, E. A. Computational Approach to Molecular Catalysis by 3d Transition Metals: Challenges and Opportunities. *Chem. Rev.* **2019**, *119*, 2453–2523.
- (5) Foscato, M.; Jensen, V. R. Automated in Silico Design of Homogeneous Catalysts. *ACS Catal.* **2020**, *10*, 2354–2377.
- (6) Curtarolo, S.; Hart, G. L.; Nardelli, M. B.; Mingo, N.; Sanvito, S.; Levy, O. The High-Throughput Highway to Computational Materials Design. *Nat. Mater.* **2013**, *12*, 191–201.
- (7) Ong, S. P.; Richards, W. D.; Jain, A.; Hautier, G.; Kocher, M.; Cholia, S.; Gunter, D.; Chevrier, V. L.; Persson, K. A.; Ceder, G. Python Materials Genomics (Pymatgen): A Robust, Open-Source Python Library for Materials Analysis. *Comput. Mater. Sci.* **2013**, *68*, 314–319.
- (8) Nørskov, J. K.; Bligaard, T. The Catalyst Genome. *Angew. Chem., Int. Ed.* **2013**, *52*, 776–777.
- (9) Meredig, B.; Agrawal, A.; Kirklin, S.; Saal, J. E.; Doak, J.; Thompson, A.; Zhang, K.; Choudhary, A.; Wolverton, C. Combinatorial Screening for New Materials in Unconstrained Composition Space with Machine Learning. *Phys. Rev. B: Condens. Matter Mater. Phys.* **2014**, *89*, 094104.
- (10) Huo, P.; Uyeda, C.; Goodpaster, J. D.; Peters, J. C.; Miller, T. F., III Breaking the Correlation between Energy Costs and Kinetic Barriers in Hydrogen Evolution via a Cobalt Pyridine-Diimine-Dioxime Catalyst. *ACS Catal.* **2016**, *6*, 6114–6123.
- (11) Grajciar, L.; Heard, C. J.; Bondarenko, A. A.; Polynski, M. V.; Meeprasert, J.; Pidko, E. A.; Nachtigall, P. Towards Operando Computational Modeling in Heterogeneous Catalysis. *Chem. Soc. Rev.* **2018**, *47*, 8307–8348.
- (12) Arockiam, P. B.; Bruneau, C.; Dixneuf, P. H. Ruthenium(II)-Catalyzed C-H Bond Activation and Functionalization. *Chem. Rev.* **2012**, *112*, 5879–5918.
- (13) Schultz, D. M.; Yoon, T. P. Solar Synthesis: Prospects in Visible Light Photocatalysis. *Science* **2014**, *343*, 1239176.
- (14) Shaffer, D. W.; Bhowmick, I.; Rheingold, A. L.; Tsay, C.; Livesay, B. N.; Shores, M. P.; Yang, J. Y. Spin-State Diversity in a Series of Co(II) PNP Pincer Bromide Complexes. *Dalton Trans* **2016**, *45*, 17910–17917.
- (15) Tsay, C.; Yang, J. Y. Electrocatalytic Hydrogen Evolution under Acidic Aqueous Conditions and Mechanistic Studies of a Highly Stable Molecular Catalyst. *J. Am. Chem. Soc.* **2016**, *138*, 14174–14177.
- (16) Schilling, M.; Patzke, G. R.; Hutter, J.; Luber, S. Computational Investigation and Design of Cobalt Aqua Complexes for Homogeneous Water Oxidation. *J. Phys. Chem. C* **2016**, *120*, 7966–7975.
- (17) Ashley, D. C.; Jakubikova, E. Ironing out the Photochemical and Spin-Crossover Behavior of Fe (II) Coordination Compounds with Computational Chemistry. *Coord. Chem. Rev.* **2017**, *337*, 97–111.
- (18) Bowman, D. N.; Bondarev, A.; Mukherjee, S.; Jakubikova, E. Tuning the Electronic Structure of Fe(II) Polypyridines via Donor Atom and Ligand Scaffold Modifications: A Computational Study. *Inorg. Chem.* **2015**, *54*, 8786–8793.
- (19) Yella, A.; Lee, H. W.; Tsao, H. N.; Yi, C. Y.; Chandiran, A. K.; Nazeeruddin, M. K.; Diau, E. W. G.; Yeh, C. Y.; Zakeeruddin, S. M.; Gratzel, M. Porphyrin-Sensitized Solar Cells with Cobalt (II/III)-Based Redox Electrolyte Exceed 12% Efficiency. *Science* **2011**, *334*, 629–634.
- (20) Kuttipillai, P. S.; Zhao, Y. M.; Traverse, C. J.; Staples, R. J.; Levine, B. G.; Lunt, R. R. Phosphorescent Nanocluster Light-Emitting Diodes. *Adv. Mater.* **2016**, *28*, 320–326.
- (21) Linfoot, C. L.; Leitl, M. J.; Richardson, P.; Rausch, A. F.; Chepelin, O.; White, F. J.; Yersin, H.; Robertson, N. Thermally Activated Delayed Fluorescence (TADF) and Enhancing Photoluminescence Quantum Yields of Cu-I(Diimine)(Diphosphine)(+) Complexes-Photophysical, Structural, and Computational Studies. *Inorg. Chem.* **2014**, *53*, 10854–10861.
- (22) Swart, M.; Costas, M. *Spin States in Biochemistry and Inorganic Chemistry: Influence on Structure and Reactivity*; John Wiley & Sons, 2015.
- (23) Meyer, B.; Sawatlon, B.; Heinen, S.; von Lilienfeld, O. A.; Corminboeuf, C. Machine Learning Meets Volcano Plots: Computational Discovery of Cross-Coupling Catalysts. *Chem. Sci.* **2018**, *9*, 7069–7077.
- (24) Weymuth, T.; Reiher, M. Inverse Quantum Chemistry: Concepts and Strategies for Rational Compound Design. *Int. J. Quantum Chem.* **2014**, *114*, 823–837.
- (25) Jiang, W.; DeYonker, N. J.; Wilson, A. K. Multireference Character for 3d Transition-Metal-Containing Molecules. *J. Chem. Theory Comput.* **2012**, *8*, 460–468.
- (26) Wang, J.; Manivasagam, S.; Wilson, A. K. Multireference Character for 4d Transition Metal-Containing Molecules. *J. Chem. Theory Comput.* **2015**, *11*, 5865–5872.
- (27) DeYonker, N. J.; Peterson, K. A.; Steyl, G.; Wilson, A. K.; Cundari, T. R. Quantitative Computational Thermochemistry of Transition Metal Species. *J. Phys. Chem. A* **2007**, *111*, 11269–11277.
- (28) Zhang, W.; Truhlar, D. G.; Tang, M. Tests of Exchange-Correlation Functional Approximations against Reliable Experimental Data for Average Bond Energies of 3d Transition Metal Compounds. *J. Chem. Theory Comput.* **2013**, *9*, 3965–3977.
- (29) Gagliardi, L.; Truhlar, D. G.; Li Manni, G.; Carlson, R. K.; Hoyer, C. E.; Bao, J. L. Multiconfiguration Pair-Density Functional Theory: A New Way to Treat Strongly Correlated Systems. *Acc. Chem. Res.* **2017**, *50*, 66–73.
- (30) Phung, Q. M.; Feldt, M.; Harvey, J. N.; Pierloot, K. Toward Highly Accurate Spin State Energetics in First-Row Transition Metal Complexes: A Combined CASPT2/Cc Approach. *J. Chem. Theory Comput.* **2018**, *14*, 2446–2455.
- (31) Singh, S. K.; Eng, J.; Atanasov, M.; Neese, F. Covalency and Chemical Bonding in Transition Metal Complexes: An Ab Initio Based Ligand Field Perspective. *Coord. Chem. Rev.* **2017**, *344*, 2–25.

- (32) Smith, J. S.; Nebgen, B. T.; Zubatyuk, R.; Lubbers, N.; Devereux, C.; Barros, K.; Tretiak, S.; Isayev, O.; Roitberg, A. E. Approaching Coupled Cluster Accuracy with a General-Purpose Neural Network Potential through Transfer Learning. *Nat. Commun.* **2019**, *10*, 2903.
- (33) Duan, C.; Liu, F.; Nandy, A.; Kulik, H. J. Data-Driven Approaches Can Overcome the Cost-Accuracy Tradeoff in Multi-reference Diagnostics. *J. Chem. Theory Comput.* **2020**, *16*, 4373–4387.
- (34) Collins, C. R.; Gordon, G. J.; von Lilienfeld, O. A.; Yaron, D. J. Constant Size Descriptors for Accurate Machine Learning Models of Molecular Properties. *J. Chem. Phys.* **2018**, *148*, 241718.
- (35) Bleiziffer, P.; Schaller, K.; Riniker, S. Machine Learning of Partial Charges Derived from High-Quality Quantum-Mechanical Calculations. *J. Chem. Inf. Model.* **2018**, *58*, 579–590.
- (36) De, S.; Bartok, A. P.; Csanyi, G.; Ceriotti, M. Comparing Molecules and Solids across Structural and Alchemical Space. *Phys. Chem. Chem. Phys.* **2016**, *18*, 13754–13769.
- (37) Ward, L.; Agrawal, A.; Choudhary, A.; Wolverton, C. A General-Purpose Machine Learning Framework for Predicting Properties of Inorganic Materials. *npj Comput. Mater.* **2016**, *2*, 16028.
- (38) Pilania, G.; Wang, C.; Jiang, X.; Rajasekaran, S.; Ramprasad, R. Accelerating Materials Property Predictions Using Machine Learning. *Sci. Rep.* **2013**, *3*, 2810.
- (39) Yao, K.; Herr, J. E.; Toth, D. W.; Mckintyre, R.; Parkhill, J. The Tensormol-0.1 Model Chemistry: A Neural Network Augmented with Long-Range Physics. *Chem. Sci.* **2018**, *9*, 2261–2269.
- (40) Behler, J. Perspective: Machine Learning Potentials for Atomistic Simulations. *J. Chem. Phys.* **2016**, *145*, 170901.
- (41) Smith, J. S.; Isayev, O.; Roitberg, A. E. ANI-1: An Extensible Neural Network Potential with DFT Accuracy at Force Field Computational Cost. *Chem. Sci.* **2017**, *8*, 3192–3203.
- (42) Zhang, L.; Han, J.; Wang, H.; Car, R.; Weinan, E. Deep Potential Molecular Dynamics: A Scalable Model with the Accuracy of Quantum Mechanics. *Phys. Rev. Lett.* **2018**, *120*, 143001.
- (43) Chmiela, S.; Tkatchenko, A.; Sauceda, H. E.; Poltavsky, I.; Schütt, K. T.; Müller, K.-R. Machine Learning of Accurate Energy-Conserving Molecular Force Fields. *Sci. Adv.* **2017**, *3*, No. e1603015.
- (44) Gaglioli, C. A.; Stoneburner, S. J.; Cramer, C. J.; Gagliardi, L. Beyond Density Functional Theory: The Multiconfigurational Approach to Model Heterogeneous Catalysis. *ACS Catal.* **2019**, *9*, 8481–8502.
- (45) Boguslawski, K.; Tecmer, P.; Legeza, O.; Reiher, M. Entanglement Measures for Single-and Multireference Correlation Effects. *J. Phys. Chem. Lett.* **2012**, *3*, 3129–3135.
- (46) Yu, H. S.; Li, S. L.; Truhlar, D. G. Perspective: Kohn-Sham Density Functional Theory Descending a Staircase. *J. Chem. Phys.* **2016**, *145*, 130901.
- (47) Cohen, A. J.; Mori-Sánchez, P.; Yang, W. Challenges for Density Functional Theory. *Chem. Rev.* **2012**, *112*, 289–320.
- (48) Becke, A. D. Perspective: Fifty Years of Density-Functional Theory in Chemical Physics. *J. Chem. Phys.* **2014**, *140*, 18A301.
- (49) Cramer, C. J.; Truhlar, D. G. Density Functional Theory for Transition Metals and Transition Metal Chemistry. *Phys. Chem. Chem. Phys.* **2009**, *11*, 10757–10816.
- (50) Guo, S.; Watson, M. A.; Hu, W.; Sun, Q.; Chan, G. K.-L. N-Electron Valence State Perturbation Theory Based on a Density Matrix Renormalization Group Reference Function, with Applications to the Chromium Dimer and a Trimer Model of Poly (P-Phenylenevinylene). *J. Chem. Theory Comput.* **2016**, *12*, 1583–1591.
- (51) Müller, T. Large-Scale Parallel Uncontracted Multireference-Averaged Quadratic Coupled Cluster: The Ground State of the Chromium Dimer Revisited. *J. Phys. Chem. A* **2009**, *113*, 12729–12740.
- (52) Pantazis, D. A. Meeting the Challenge of Magnetic Coupling in a Triply-Bridged Chromium Dimer: Complementary Broken-Symmetry Density Functional Theory and Multireference Density Matrix Renormalization Group Perspectives. *J. Chem. Theory Comput.* **2019**, *15*, 938–948.
- (53) Goodgame, M. M.; Goddard, W. A., III The "Sextuple" Bond of Chromium Dimer. *J. Phys. Chem.* **1981**, *85*, 215–217.
- (54) Lee, T. J.; Taylor, P. R. A Diagnostic for Determining the Quality of Single-Reference Electron Correlation Methods. *Int. J. Quantum Chem.* **1989**, *36*, 199–207.
- (55) Sears, J. S.; Sherrill, C. D. Assessing the Performance of Density Functional Theory for the Electronic Structure of Metal-Salens: The d(2)-Metals. *J. Phys. Chem. A* **2008**, *112*, 6741–6752.
- (56) Sears, J. S.; Sherrill, C. D. Assessing the Performance of Density Functional Theory for the Electronic Structure of Metal-Salens: The 3d(0)-Metals. *J. Phys. Chem. A* **2008**, *112*, 3466–3477.
- (57) Langhoff, S. R.; Davidson, E. R. Configuration Interaction Calculations on the Nitrogen Molecule. *Int. J. Quantum Chem.* **1974**, *8*, 61–72.
- (58) Janssen, C. L.; Nielsen, I. M. B. New Diagnostics for Coupled-Cluster and Moller-Plesset Perturbation Theory. *Chem. Phys. Lett.* **1998**, *290*, 423–430.
- (59) Nielsen, I. M. B.; Janssen, C. L. Double-Substitution-Based Diagnostics for Coupled-Cluster and Moller-Plesset Perturbation Theory. *Chem. Phys. Lett.* **1999**, *310*, 568–576.
- (60) Fogueri, U. R.; Kozuch, S.; Karton, A.; Martin, J. M. L. A Simple DFT-Based Diagnostic for Nondynamical Correlation. *Theor. Chem. Acc.* **2013**, *132*, 1291.
- (61) Tishchenko, O.; Zheng, J. J.; Truhlar, D. G. Multireference Model Chemistries for Thermochemical Kinetics. *J. Chem. Theory Comput.* **2008**, *4*, 1208–1219.
- (62) Schultz, N. E.; Zhao, Y.; Truhlar, D. G. Density Functionals for Inorganometallic and Organometallic Chemistry. *J. Phys. Chem. A* **2005**, *109*, 11127–11143.
- (63) Ramos-Cordoba, E.; Salvador, P.; Matito, E. Separation of Dynamic and Nondynamic Correlation. *Phys. Chem. Chem. Phys.* **2016**, *18*, 24015–24023.
- (64) Ramos-Cordoba, E.; Matito, E. Local Descriptors of Dynamic and Nondynamic Correlation. *J. Chem. Theory Comput.* **2017**, *13*, 2705–2711.
- (65) Grimme, S.; Hansen, A. A Practicable Real-Space Measure and Visualization of Static Electron-Correlation Effects. *Angew. Chem., Int. Ed.* **2015**, *54*, 12308–12313.
- (66) Weinert, M.; Davenport, J. W. Fractional Occupations and Density-Functional Energies and Forces. *Phys. Rev. B: Condens. Matter Mater. Phys.* **1992**, *45*, 13709–13712.
- (67) Kesharwani, M. K.; Sylvetsky, N.; Köhn, A.; Tew, D. P.; Martin, J. M. L. Do CCSD and Approximate CCSD-F12 Variants Converge to the Same Basis Set Limits? The Case of Atomization Energies. *J. Chem. Phys.* **2018**, *149*, 154109.
- (68) Sprague, M. K.; Irikura, K. K. Quantitative Estimation of Uncertainties from Wavefunction Diagnostics. In *Thom H. Dunning Jr. Highlights in Theoretical Chemistry*; Springer, 2015; pp 307–318.
- (69) Via-Nadal, M.; Rodríguez-Mayorga, M.; Ramos-Cordoba, E.; Matito, E. Singling out Dynamic and Nondynamic Correlation. *J. Phys. Chem. Lett.* **2019**, *10*, 4032–4037.
- (70) Süß, D.; Huber, S. E.; Mauracher, A. On the Impact of Multi-Reference Character of Small Transition Metal Compounds on Their Bond Dissociation Energies. *J. Chem. Phys.* **2020**, *152*, 114104.
- (71) Janet, J. P.; Kulik, H. J. Predicting Electronic Structure Properties of Transition Metal Complexes with Neural Networks. *Chem. Sci.* **2017**, *8*, 5137–5152.
- (72) Janet, J. P.; Chan, L.; Kulik, H. J. Accelerating Chemical Discovery with Machine Learning: Simulated Evolution of Spin Crossover Complexes with an Artificial Neural Network. *J. Phys. Chem. Lett.* **2018**, *9*, 1064–1071.
- (73) Nandy, A.; Duan, C.; Janet, J. P.; Gugler, S.; Kulik, H. J. Strategies and Software for Machine Learning Accelerated Discovery in Transition Metal Chemistry. *Ind. Eng. Chem. Res.* **2018**, *57*, 13973–13986.
- (74) Duan, C.; Janet, J. P.; Liu, F.; Nandy, A.; Kulik, H. J. Learning from Failure: Predicting Electronic Structure Calculation Outcomes with Machine Learning Models. *J. Chem. Theory Comput.* **2019**, *15*, 2331–2345.

- (75) Janet, J. P.; Ramesh, S.; Duan, C.; Kulik, H. J. Accurate Multiobjective Design in a Space of Millions of Transition Metal Complexes with Neural-Network-Driven Efficient Global Optimization. *ACS Cent. Sci.* **2020**, *6*, 513–524.
- (76) Gugler, S.; Janet, J. P.; Kulik, H. J. Enumeration of De Novo Inorganic Complexes for Chemical Discovery and Machine Learning. *Mol. Sys. Des. Eng.* **2020**, *5*, 139–152.
- (77) Hollett, J. W.; Gill, P. M. W. The Two Faces of Static Correlation. *J. Chem. Phys.* **2011**, *134*, 114111.
- (78) Janet, J. P.; Kulik, H. J. Resolving Transition Metal Chemical Space: Feature Selection for Machine Learning and Structure-Property Relationships. *J. Phys. Chem. A* **2017**, *121*, 8939–8954.
- (79) Janet, J. P.; Gani, T. Z. H.; Steeves, A. H.; Ioannidis, E. I.; Kulik, H. J. Leveraging Cheminformatics Strategies for Inorganic Discovery: Application to Redox Potential Design. *Ind. Eng. Chem. Res.* **2017**, *56*, 4898–4910.
- (80) Nandy, A.; Zhu, J.; Janet, J. P.; Duan, C.; Getman, R. B.; Kulik, H. J. Machine Learning Accelerates the Discovery of Design Rules and Exceptions in Stable Metal–Oxo Intermediate Formation. *ACS Catal.* **2019**, *9*, 8243–8255.
- (81) Janet, J. P.; Duan, C.; Yang, T.; Nandy, A.; Kulik, H. J. A Quantitative Uncertainty Metric Controls Error in Neural Network-Driven Chemical Discovery. *Chem. Sci.* **2019**, *10*, 7913–7922.
- (82) Janet, J. P.; Liu, F.; Nandy, A.; Duan, C.; Yang, T.; Lin, S.; Kulik, H. J. Designing in the Face of Uncertainty: Exploiting Electronic Structure and Machine Learning Models for Discovery in Inorganic Chemistry. *Inorg. Chem.* **2019**, *58*, 10592–10606.
- (83) Ioannidis, E. I.; Kulik, H. J. Towards Quantifying the Role of Exact Exchange in Predictions of Transition Metal Complex Properties. *J. Chem. Phys.* **2015**, *143*, 034104.
- (84) Ganzenmüller, G.; Berkäine, N.; Fouqueau, A.; Casida, M. E.; Reiher, M. Comparison of Density Functionals for Differences between the High-(T 2 G 5) and Low-(a 1 G 1) Spin States of Iron (II) Compounds. IV. Results for the Ferrous Complexes [Fe(L)(Nhs 4)]. *J. Chem. Phys.* **2005**, *122*, 234321.
- (85) Droghetti, A.; Alfè, D.; Sanvito, S. Assessment of Density Functional Theory for Iron (II) Molecules across the Spin-Crossover Transition. *J. Chem. Phys.* **2012**, *137*, 124303.
- (86) Mortensen, S. R.; Kepp, K. P. Spin Propensities of Octahedral Complexes from Density Functional Theory. *J. Phys. Chem. A* **2015**, *119*, 4041–4050.
- (87) Pierloot, K. The CASPT2Method in Inorganic Electronic Spectroscopy: From Ionic Transition Metal to Covalent Actinide Complexes*. *Mol. Phys.* **2003**, *101*, 2083–2094.
- (88) Pierloot, K.; Phung, Q. M.; Domingo, A. Spin State Energetics in First-Row Transition Metal Complexes: Contribution of (3s3p) Correlation and Its Description by Second-Order Perturbation Theory. *J. Chem. Theory Comput.* **2017**, *13*, 537–553.
- (89) Flöser, B. M.; Guo, Y.; Ripplinger, C.; Tuczak, F.; Neese, F. Detailed Pair Natural Orbital-Based Coupled Cluster Studies of Spin Crossover Energetics. *J. Chem. Theory Comput.* **2020**, *16*, 2224–2235.
- (90) Feldt, M.; Phung, Q. M.; Pierloot, K.; Mata, R. A.; Harvey, J. N. Limits of Coupled-Cluster Calculations for Non-Heme Iron Complexes. *J. Chem. Theory Comput.* **2019**, *15*, 922–937.
- (91) Zhang, D.; Truhlar, D. G. Spin Splitting Energy of Transition Metals: A New, More Affordable Wave Function Benchmark Method and Its Use to Test Density Functional Theory. *J. Chem. Theory Comput.* **2020**, *16*, 4416–4428.
- (92) Mizukami, W.; Kurashige, Y.; Yanai, T. Communication: Novel Quantum States of Electron Spins in Polycarbenes from Ab Initio Density Matrix Renormalization Group Calculations. *J. Chem. Phys.* **2010**, *133*, 091101.
- (93) Shen, J.; Xu, E.; Kou, Z.; Li, S. New Coupled Cluster Approaches Based on the Unrestricted Hartree–Fock Reference for Treating Molecules with Multireference Character. *Phys. Chem. Chem. Phys.* **2011**, *13*, 8795–8804.
- (94) Herbol, H. C.; Hu, W.; Frazier, P.; Clancy, P.; Poloczek, M. Efficient Search of Compositional Space for Hybrid Organic–Inorganic Perovskites via Bayesian Optimization. *npj Comput. Mater.* **2018**, *4*, 51.
- (95) Häse, F.; Roch, L. M.; Kreisbeck, C.; Aspuru-Guzik, A. Phoenics: A Bayesian Optimizer for Chemistry. *ACS Cent. Sci.* **2018**, *4*, 1134–1145.
- (96) Duan, C.; Liu, F.; Nandy, A.; Kulik, H. J. Semi-Supervised Machine Learning Enables the Robust Detection of Multireference Character at Low Cost. *J. Phys. Chem. Lett.* **2020**, *11*, 6640–6648.
- (97) <http://www.petachem.com> (accessed 2020-07-19).
- (98) Ufimtsev, I. S.; Martinez, T. J. Quantum Chemistry on Graphical Processing Units. 3. Analytical Energy Gradients, Geometry Optimization, and First Principles Molecular Dynamics. *J. Chem. Theory Comput.* **2009**, *5*, 2619–2628.
- (99) Ioannidis, E. I.; Gani, T. Z. H.; Kulik, H. J. molSimplify: A Toolkit for Automating Discovery in Inorganic Chemistry. *J. Comput. Chem.* **2016**, *37*, 2106–2117.
- (100) KulikGroup. molSimplify Documentation. <http://molsimplify.mit.edu> (accessed 2020-07-19).
- (101) Liu, F.; Duan, C.; Kulik, H. J. Multirefpredict. <https://github.com/hjkgrp/Multirefpredict> (accessed 2020-07-19).
- (102) MolSSI. QC Engine. <https://github.com/MolSSI/QCEngine> (accessed 2020-07-19).
- (103) Stephens, P. J.; Devlin, F. J.; Chabalowski, C. F.; Frisch, M. J. Ab Initio Calculation of Vibrational Absorption and Circular Dichroism Spectra Using Density Functional Force Fields. *J. Phys. Chem.* **1994**, *98*, 11623–11627.
- (104) Becke, A. D. Density-Functional Thermochemistry. III. The Role of Exact Exchange. *J. Chem. Phys.* **1993**, *98*, 5648–5652.
- (105) Lee, C.; Yang, W.; Parr, R. G. Development of the Colle-Salvetti Correlation-Energy Formula into a Functional of the Electron Density. *Phys. Rev. B: Condens. Matter Mater. Phys.* **1988**, *37*, 785–789.
- (106) Hay, P. J.; Wadt, W. R. Ab Initio Effective Core Potentials for Molecular Calculations. Potentials for the Transition Metal Atoms Sc to Hg. *J. Chem. Phys.* **1985**, *82*, 270–283.
- (107) Saunders, V. R.; Hillier, I. H. A “Level-Shifting” Method for Converging Closed Shell Hartree–Fock Wave Functions. *Int. J. Quantum Chem.* **1973**, *7*, 699–705.
- (108) Bergstra, J.; Yamins, D.; Cox, D. D. In Hyperopt: A Python Library for Optimizing the Hyperparameters of Machine Learning Algorithms. *Proceedings of the 12th Python in science conference*; pp 13–20.
- (109) Breiman, L. Random Forests. *Mach. Learn.* **2001**, *45*, 5–32.
- (110) Guyon, I.; Elisseeff, A. An Introduction to Variable and Feature Selection. *Journal of Machince Learning Research* **2003**, *3*, 1157–1182.
- (111) Pedregosa, F.; Varoquaux, G.; Gramfort, A.; Michel, V.; Thirion, B.; Grisel, O.; Blondel, M.; Prettenhofer, P.; Weiss, R.; Dubourg, V. Scikit-Learn: Machine Learning in Python. *Journal of Machine Learning Research* **2011**, *12*, 2825–2830.
- (112) Chollet, F. Keras. <https://keras.io> (accessed 2020-07-19).
- (113) Abadi, M.; Agarwal, A.; Barham, P.; Brevdo, E.; Chen, Z.; Citro, C.; Corrado, G. S.; Davis, A.; Dean, J.; Devin, M.; et al. Tensorflow: Large-Scale Machine Learning on Heterogeneous Systems; 2015.
- (114) Srivastava, N.; Hinton, G.; Krizhevsky, A.; Sutskever, I.; Salakhutdinov, R. Dropout: A Simple Way to Prevent Neural Networks from Overfitting. *Journal of Machine Learning Research* **2014**, *15*, 1929–1958.
- (115) Hinton, G. E.; Srivastava, N.; Krizhevsky, A.; Sutskever, I.; Salakhutdinov, R. R. Improving Neural Networks by Preventing Co-Adaptation of Feature Detectors. *arXiv* **2012**, 1207.0580.